KeA1
CHINESE ROOTS
GLOBAL IMPACT

Contents lists available at ScienceDirect

Biomedical Technology

journal homepage: www.keaipublishing.com/en/journals/biomedical-technology



Research Paper

Direct ink writing of bioactive PCL/laponite bone Implants: Engineering the interplay of design, process, structure, and function *



Hongyi Chen ^{a,b,*}, Rui Cheng ^c, Se Hun Chung ^a, Arsalan Marghoub ^a, Hui Zhong ^d, Guohao Fang ^e, Stavroula Balabani ^a, Lucy Di-Silvio ^c, Jie Huang ^{a,**}

- ^a Department of Mechanical Engineering, University College London, London, United Kingdom
- ^b Department of Computer Science, University College London, London, United Kingdom
- ^c Faculty of Dentistry, Oral & Craniofacial Sciences, King's College London, London, United Kingdom
- d College of Civil and Transportation Engineering, Guangdong Province Key Laboratory of Durability for Marine Civil Engineering, Shenzhen Key Laboratory for Low-carbon Construction Material and Technology, Shenzhen University, Shenzhen, 518060, China
- ^e Institute for Advanced Study, Shenzhen University, Shenzhen, 518060, China

ARTICLE INFO

Keywords: 3D printing Mechanical properties 3D assessment Micro-CT Cell activities

ABSTRACT

Direct ink writing (DIW) is a room-temperature extrusion-based 3D printing technique that enables the fabrication of dense, customizable implants from viscous inks with precise spatial control. In this study, we present an engineering design framework for DIW-printed PCL/Laponite composites by tuning ink formulations and printing orientations to systematically investigate and control the complex interplay between shape fidelity, mechanical performance, and cellular response. Our findings show that printing at 0° orientation enhances filament-aligned surface topographies, which guide osteoblast attachment and significantly promote cell proliferation and mineralization. In contrast to previous studies using fused deposition modeling (FDM), we observe that printing at 90° orientation (perpendicular to the tensile load direction) results in higher mechanical performance due to improved filament bonding. Increasing Laponite loading (up to 30 %) improves shape retention by increasing ink viscosity, raises Young's modulus by up to 110 %, and enhances surface bioactivity by introducing hydrophilic and bioactive cues. This study provides a tunable strategy for engineering bioactive and surface-active implants for the clinical need for non-load-bearing orthopaedic applications where structural integrity, surface-mediated osteointegration, and customized geometry are clinically essential.

1. Introduction

Using 3D printing for biomedical applications has gained popularity in recent years, as it enables the fabrication of complex implants with customized architecture specific to each patient and clinical condition [1–5]. Among 3D printing techniques, direct ink writing (DIW), which involves directly extruding relatively viscous material through a moving nozzle, has been widely adopted in the biomedical field [6–10]. It operates at room temperature, allowing a broad selection of biomaterials, temperature-sensitive drugs, and biomolecules. PCL is an FDA-approved polymer popular for tissue engineering implants due to

its biocompatibility, biodegradability, and high permeability to drugs [11–13]. However, its Young's modulus is lower than natural bone tissues, and its osteoconductive potential is limited. Laponite, a type of nanoclay, offers high surface area and unique physicochemical characteristics, making it particularly effective in enhancing the local cell-material microenvironment [14].

Printability of inks is an important property for 3D printing as the shape of the printed products influences their integration and function [5,15–17]. Shape fidelity is commonly used as an indicator of printability, typically assessed by the shape and size of individual filaments or pores in porous lattice structures. It has been shown to be largely

Peer review under the responsibility of the Editorial Board of Biomedical Technology.

https://doi.org/10.1016/j.bmt.2025.100101

Received 1 August 2025; Received in revised form 12 August 2025; Accepted 13 August 2025 Available online 2 September 2025

^{*} This study does not involve human participants, human data or human tissue, and does not contain any individual persons data, therefore the consent to participate is not applicable.

^{*} Corresponding author. Department of Computer Science, University College London, London, United Kingdom.

^{**} Corresponding author. Department of Mechanical Engineering, University College London, London, United Kingdom *E-mail address:* hongyi.chen.16@ucl.ac.uk (H. Chen).

influenced by ink rheology, which can be modulated through tailored formulations. For example, low-dimensional materials, such as nanofillers, have been used to tune ink rheology and, enhance printability and functions [15,18–20]. However, current rheology and printability studies focus on hydrogel-based inks, leaving the realm of organic solvent-based polymer inks largely unexplored. In addition, current printability assessment is based on porous implant structures, rather than solid implants where adjacent filaments are bonded. Consequently, there is a pressing need to delve into the rheology and printability of 3D printed organic solvent-based polymer inks for solid structures.

In addition to shape fidelity, the mechanical properties of 3D-printed bone implants are vital for ensuring stability under mechanical load while preventing stress shielding. [21–23]. These properties are influenced by both ink formulation and printing parameters. Nanofillers, for instance, enhance stress dissipation within the polymer, while filament orientation affects interfacial bonding in 3D printed products [24–28]. However, most studies investigate the effect of ink formulations and properties or printing parameters on mechanical properties individually. This study systematically investigates how these factors collectively influence shape fidelity and mechanical properties. In addition, previous research has predominantly focused on FDM, and limited attention has been given to DIW in this context.

While all the engineering aspects mentioned above are important for high-performance printing, cell response is crucial for biological applications of printed products [23,29,30]. Ink formulation, the resulting 3D architecture, and surface topography all play interconnected roles in guiding cellular behavior. In particular, both the mechanical performance and biological response of printed structures are shaped by the combined effects of material composition and printing parameters. A detailed understanding of this structure-property-cell response relationship in 3D printed dense implants is especially important for dense, surface-active implants used in non-load-bearing bone repair applications, such as guided bone regeneration (GBR), craniomaxillofacial reconstruction, and defect filling [31-33]. In these scenarios, implants must provide structural stability while supporting surface-mediated osteointegration. Therefore, elucidating the interplay between ink design and print orientation is essential to optimizing direct ink writing (DIW) for such clinical applications.

This study pioneers in researching the interplay between compositions, rheology, printing design, shape fidelity, mechanical properties and cell response of 3D printed structures with DIW in an integrated manner. The PCL/LP nanocomposite dumbbell-shaped specimens were 3D printed with 2 orientations (0 $^{\circ}$ and 90 $^{\circ}$) and different LP loading

concentrations: 0%, 10%, 20% and 30%. The rheological properties of the inks were characterized and the shape fidelity, mechanical properties, and *in vitro* assessment with human osteoblast (HOB) cells were conducted. Fig. 1 illustrates the interplay between ink formulation & properties, printing design on the shape retention, mechanical properties, and cellular responses of the printed products.

2. Materials and methodologies

2.1. Ink preparation

PCL pellets (molecular weight: 80 kDa) were purchased from Sigma-Aldrich and used as the polymeric matrix. Laponite® (LP) was kindly supplied by BYK Additives Ltd. Dichloromethane (DCM: CH_2Cl_2) was purchased from VWR Chemicals.

To make the PCL polymer-based ink, 50 % w/v of PCL was dissolved in DCM for 4h under magnetic stirring. The concentration of 50 % w/v of PCL makes the ink printable while also accommodating the increase in viscosity with the incorporation of nanofillers. For nanofiller-loaded composite inks, weighed bioactive nanofiller particles were mixed in DCM solvent for 10 min under magnetic stirring prior to dissolving PCL for a homogenous dispersion. Then weighed PCL pellets were added gradually to reach 50 % w/v. All inks were subject to ultrasonic bath for 2 min to disperse the particles and then centrifuged (2000 rpm) for 2 min to remove air bubbles. Three nanofiller/(PCL + nanofiller) concentrations (10 %, 20 % and 30 %) were used for making PCL/LP composite inks. Filler loading density higher than 30 % can cause nozzle clogging issues and was not used in subsequent assessments.

2.2. Rheological tests

The rheological properties of the PCL/LP inks at 20 °C were assessed using a rotational rheometer (Discovery HR, TA Instruments) in order to investigate the effect of LP loading on the ink rheology. Steady and small amplitude oscillatory shear tests were conducted with a 40 mm plateplate sandblasted geometry and a gap of 400 μm . Shear viscosity profiles of the inks were obtained with rotational flow sweep tests in the shear rate range of 0.1–100 s $^{-1}$. A solvent trap was used to minimize drying during testing. The relatively short range of shear rates (0.1–100 s $^{-1}$) was selected to reduce measurement time and further limit drying, contributing to repeatable measurements. The storage modulus G' of the inks was measured in the linear viscoelastic region, using frequency sweeps in the range of 0.1–100 Hz and a fixed strain

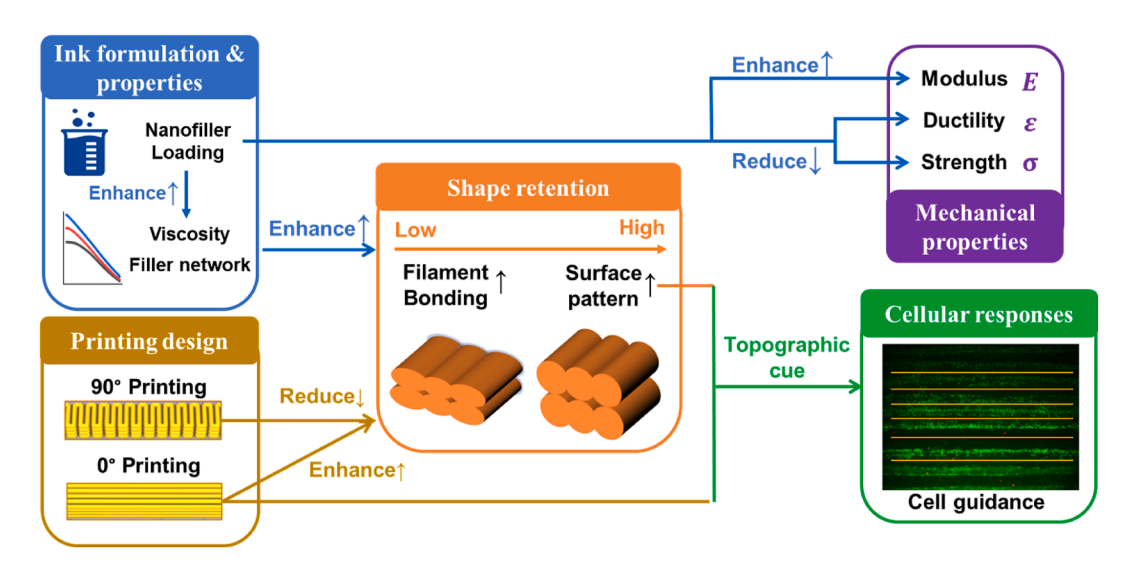


Fig. 1. The interplay between the effect of nanofiller loading and printing orientation on the properties of the printed product including shape retention, mechanical properties and cellular response investigated in this study.

amplitude of 1 %. The strain amplitude of 1 % is within the linear viscoelastic region of the inks as determined by preliminary amplitude sweep tests.

2.3. Fourier-transform infrared spectroscopy (FTIR)

The functional groups within the fillers and 3D printed PCL-based composites and were analyzed by FTIR spectrometer (PerkinElmer 2000, PerkinElmer, Inc., Waltham, Massachusetts, USA). The spectra were collected by 64 scans with the wavelength ranging from 400 to $4000~{\rm cm}^{-1}$ and resolution of $4~{\rm cm}^{-1}$. Characteristic peaks were compared to identify molecular interactions and compositional differences between neat PCL and PCL/Laponite composites.

2.4. X-ray diffraction (XRD)

XRD patterns of the 3D printed specimens were determined using a Rigaku Miniflex 600 X-ray diffractometer. CuK α radiation and operating power of 40 kV and 15 mA, respectively, were used throughout. The diffraction patterns were collected at room temperature over the 2 θ range of 3–40° with a step size of 0.02° and a scan rate of 5°/min. The degree of crystallinity (X_C) of the specimens was calculated by deconvoluting peaks of amorphous and crystalline phases from their diffraction patterns according to the following Equation 1 [34]:

$$X_C = \frac{I_C}{I_C + I_A} \times 100\% \tag{1}$$

Where I_C is the total integrated crystalline area of crystalline PCL peaks determined from the deconvolution of the XRD results and I_A is the amorphous PCL area under the halo centred at 21.3° .

2.5. Differential scanning calorimetry (DSC)

The thermal behavior of the 3D printed specimens was assessed with DSC using Q2000 (TA Instruments) to examine the effect of orientations and nanofiller loading on the crystallinity of PCL. 3D printed PCL/LP composite specimens with different nanofiller loading concentrations and orientations (0° and 90°) were examined. The specimens were cut into a disk shape of around 4 mm in diameter and 2 mm in thickness and the weight was kept at 5–6 mg. The standard heat-cool-heat method was used with a ramp rate of 10 °C/min and an isothermal period of 15 min in between each ramp. The first heating cycle started from an ambient temperature of 20 °C and heating to 150 °C. Then the specimens were cooled down to -20 °C, to ensure complete crystallization of PCL, and reheated to 150 °C. The degree of crystallinity ($X_{\rm C}$) was calculated as [351]:

$$X_C = \frac{\Delta H_F}{\Delta H_F^0} \times 100\% \tag{2}$$

Where ΔH_F is the enthalpy of fusion measured at the melting point

during the first heating and ΔH_F^0 is the enthalpy of melting of 100 % crystalline PCL and 135 J/g was used [35].

2.6. 3D printing dumbbell specimens

The 3D printing process was performed with a DIW printer (Fig. 2A) that was modified from a commercial FDM printer (Prusa i3). The original thermoplastic extruder was replaced with a syringe pump extruder driven by the same NEMA-17 stepper motor, enabling mechanical extrusion of soft materials such as polymer-based organic solutions. This modification retains the original printer's XYZ motion control system and is fully compatible with common G-code generation software, including Cura used in this study. Retraction was disabled to maintain a consistent extrusion flow, critical for DIW printing of viscous materials. Additionally, G-code was manually edited to align the end point of each layer with the starting point of the next, minimizing nozzle travel and maintaining flow consistency. The print speed for all specimens was set as 7.5 mm/s which is optimized to balance efficiency and print quality. The nozzle diameter was 0.6 mm, the layer height was 0.4 mm to facilitate filament bonding All printing was performed at room temperature (20 °C), with a constant print speed of 7.5 mm/s, optimized for extrusion stability and shape fidelity. No fill gap was applied, ensuring full filament contact to form solid, fused structures. Frosted glass coated with poly(vinyl alcohol) hydrogel was used as substrate as it facilitates adhesion between the printed structure and the substrate. The PCL/LP nanocomposite inks were 3D printed into dumbbell specimens (ASTM D638 Type IV, scaled down 50 %). The total length of the specimens was around 58 mm, the length of the narrow middle part was 16 mm, and the gauge length and width were 12 mm and 3 mm respectively. Two filament orientations, 0° and 90°, which represent the extremes of filament alignment were printed for tensile testing (Fig. 2B (C)). They provide a clear contrast as they represent the extremes of alignment, and a baseline understanding of how alignment influences the properties of the printed implants.

2.7. Structural assessment

Micro-CT scanning (Nikon XT H 225 ST) was used to assess the gauge section of the 3D printed PCL/LP dumbbell-shaped specimens before and after tensile testing in a 3D manner. Circular (360°) scans were performed on the printed specimens using a high-resolution micro-computed tomography (micro-CT) system. The voxel size was set to 6.5 μm , providing fine spatial resolution suitable for evaluating filament fidelity and internal morphology. The X-ray source power was set at 6 W to minimize beam-induced blurring while remaining below the voxel resolution threshold. Beam energy was optimized at $\sim\!60$ kV to ensure adequate penetration through the polymer-composite structures while maintaining high contrast between the material and background. The contrast range between the minimum grayscale within the specimen and the detector baseline, as well as between the maximum grayscale and

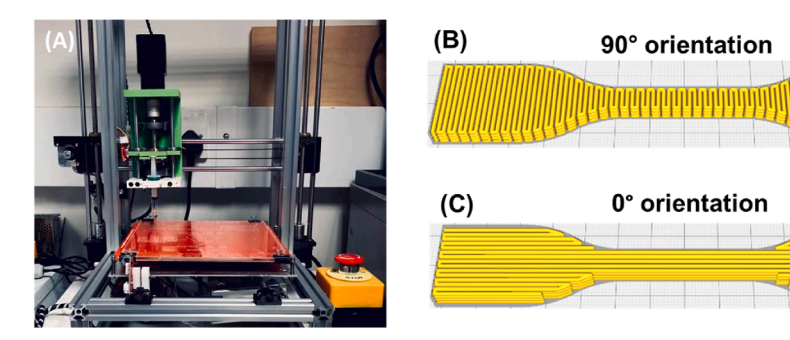


Fig. 2. (A) The custom-made DIW 3D printer used in the lab. (B) and (C) The printing paths for the dumbbell-shaped specimen with 90° and 0° orientations respectively in the preview mode of Ultimaker Cura.

surrounding background, exceeded 4000 grayscale units—ensuring clear segmentation during image reconstruction. A gain of 30 dB was used to limit electronic noise, while a relatively long exposure time of 1 s was chosen to enhance brightness and compensate for the lower gain. This produced image grayscale values in the range of approximately 18,000 to 56,000. Before scanning, detector calibration and shading correction were performed. Shading correction compensates for nonuniformities in detector sensitivity and beam intensity. Image reconstruction was performed in CT agent where the images taken from micro-CT scanning were transformed into volumetric data. First the images at the starting point and final point were checked to ensure that the specimens were stable during scanning. The beam hardening and ring artifact were minimized during reconstruction. Avizo 3D (Thermo Fisher Scientific, Mass, USA) was used to analyse the volumetric data acquired by micro-CT, visualize the structures of interest and perform measurements. Briefly, the region of interest was initially segmented by applying a grayscale threshold to differentiate the material from the background, defining the primary volume. To eliminate noise and background artifacts, the Pick & Move tool was employed to isolate only interconnected voxel regions, thereby removing unconnected background voxels. The Remove Island function was subsequently used to discard small voxel clusters attached to the surface that were not part of

Particle size distribution analysis was conducted using VGSTUDIO MAX based on micro-CT data. Due to beam path variation during scanning, minor grayscale inconsistencies may remain even after reconstruction. To address this, VGSTUDIO MAX's local contrast-based segmentation was used, which evaluates voxel intensity relative to its neighboring region, enhancing segmentation accuracy. Particles were identified using a standard deviation threshold of 0.6 in the VGpore module, selecting voxels with grayscale values exceeding the local mean by more than 0.6 standard deviations. This method allows for precise identification of microstructural features while reducing false positives from grayscale noise.

The porosity P_t of 3D printed structures is calculated as:

$$P_t = \frac{V_p}{V_c} \times 100\% \tag{3}$$

Where V_p is the volume of pores and V_t is the total volume of the structure.

The surface morphology of 3D printed PCL/LP specimens was analyzed using scanning electron microscopy (SEM) (Zeiss GeminiSEM 360, Carl Zeiss AG, Germany). Imaging was conducted on the gauge regions of the PCL/LP constructs both before and after tensile testing, as well as after seeding with human osteoblast (HOB) cells. The specimens were sputter-coated with gold nanoparticles prior to SEM imaging. SEM imaging was carried out at a voltage of 5 kV using a secondary electron (SE) detector to capture high-resolution topographic features.

The nanoscale surface roughness of the printed specimens was characterized using an atomic force microscope (AFM) (Bruker Dimension Icon) operating in tapping mode. Specimens were affixed to magnetic sample disks and scanned under ambient conditions. Each sample was scanned over a 30 $\mu m \times 30~\mu m$ area at a scan rate using a silicon probe Topographical images were captured and analyzed using Bruker's NanoScope Analysis software and the root mean square (RMS) roughness was calculated from at least three different surface regions per sample, and the mean and standard deviation were reported for each group.

Microscale surface roughness of the printed specimens was assessed using a Keyence VHX-X1 digital microscope operated at $500 \times$ magnification. 3D surface reconstruction was performed using the system's built-in depth composition and profilometry functions. Representative surface regions (\sim 2000 μ m \times 2000 μ m) were imaged, avoiding edge defects and interfacial discontinuities. For each group, three specimens were analyzed, and three measurements per specimen were taken to

ensure reproducibility. Root mean square (RMS) roughness measurements were calculated using the microscope's integrated software, and results were reported as mean \pm standard deviation.

2.8. Water contact angle measurement

The surface wettability of the printed specimens was assessed using a contact angle goniometer (Ossila, UK) equipped with a high-resolution camera and image analysis software. Samples were placed on a leveled stage, and $2\,\mu L$ droplets of deionized water were carefully dispensed onto the surface using a microliter syringe. Contact angle images were captured immediately after droplet deposition to minimize evaporation effects. Measurements were conducted at room temperature under ambient conditions. For each sample group, three different specimens were tested, and three measurements were taken per specimen at different surface locations. The static contact angle was determined using Ossila's built-in drop shape analysis software, which applied a tangent-fitting method to the droplet profile. The mean and standard deviation were reported for each group.

2.9. Tensile testing

Uniaxial tensile tests, according to the ASTM D638-14 standard (specimens scaled down 50 %), were conducted on the dumbbell specimens using a universal testing machine (Instron-5969) at a displacement rate of 10 mm/min. All tests were conducted at room temperature (20 °C) with a 50 kN load cell. The cross-sectional area and gauge length of each specimen were used to calculate the engineering stress and strain to generate a stress-strain plot. The Young's modulus (E) was measured as the ratio of stress over the strain in the linear region. Ultimate tensile strength (UTS) is the maximum stress prior to fracture and fracture strain (FS) is the strain measured at the breakage of the specimen. A sample size of 5 was used.

2.10. In vitro cell culture

Human osteoblast cells (PromoCell Catalogue No: C-12720) were seeded at a concentration of $1x10^5$ per specimen/well on the 3D printed specimens to assess cell viability and morphology of cells. Cells were incubated in HOB media: Dulbecco's modified Eagle's medium (DMEM; Hyclone, USA) supplemented with 10 % fetal bovine serum (Hyclone) and 1 % penicillin–streptomycin (Hyclone). The 3D printed specimens were sterilized by soaking with 70 % ethanol for 24 h. Prior to cell seeding, the specimens are then submerged in human osteoblast culture media at 37 $^{\circ}$ C at 5 % CO₂ for 24 h to facilitate cell adhesion.

2.11. Cell viability assessment

Cell viability was assessed using a LIVE/DEADTM Viability/Cytotoxicity Kit (Thermo Fisher Scientific, Waltham, MA, USA) after 7 days of cell culture. The kit consists of calcein AM which stains live cells and Ethidium homodimer-1 which stains dead cells. Staining solutions were made by adding calcein AM (1 μ l/ml) and Ethidium homodimer-1 (1 μ l/ml) in HOB culture media. HOB-seeded samples were rinsed in PBS, submerged in staining solutions for 30 min and then imaged with an Olympus IX51 fluorescent microscope. ImageJ software was used to display and merge images of live and dead cells of the same location to enable counting and viability estimation.

2.12. Cell proliferation assessment

Proliferation assessment was conducted using alamarBlueTM assay, as previously described [36]. Implants made from PCL-based materials were seeded with 1×10^4 HOB cells each, and their proliferation was evaluated over a 15-day period. Cell-seeded implants were placed in 24-well plates and maintained in culture medium for the designated

time points. At each time point, the existing medium was replaced with a 10~% AlamarBlue $^{\rm TM}$ solution, and the implants were incubated for 4 h. Negative controls consisted of 10~% AlamarBlue $^{\rm TM}$ solution without cells, while tissue culture plastic seeded with cells served as the positive control. Following incubation, $100~\mu L$ of the medium from each well was transferred to a 96-well plate, and absorbance was measured using a microplate reader at a test wavelength of 570 nm and a reference wavelength of 630 nm (Dynex Technologies, Chantilly, VA, USA). The results demonstrated absorbance changes over 15 days, reflecting cell proliferation in the PCL-based implants.

2.13. Cell mineralization assessment

Calcium deposition on HOB-seeded 3D-printed implants was evaluated using Alizarin Red S staining on day 16 and day 26. At each time point, implants were washed with PBS, fixed with 10 % formal saline, and rinsed with deionized water. The fixed specimens were stained with 1 mL of 2 % Alizarin Red S solution for 15 min and then washed with 50 % ethanol. Images of the stained implants were captured for qualitative analysis. Quantitative assessments were conducted by adapting a previously published protocol [36,37]. Bound stain on the implants was dissolved with 1 mL of 10 % cetylpyridinium chloride (CPC) solution, and 100 µL aliquots of the supernatant were transferred to a 96-well plate. Absorbance was measured using a microplate reader (Opsys MRTM 96-well microplate reader, Dynex Technologies, Chantilly, VA, USA) at 570 nm. Serial dilutions of Alizarin Red S in CPC solution were used to construct a standard curve. Calcium deposition was calculated based on the molar ratio of Alizarin Red S to calcium, where 1 mol of Alizarin Red S binds to 2 mol of calcium [38]. Mineralization results were expressed as µmoles of calcium per well, with measurements from unseeded implants (blank controls) subtracted from the calcium deposition measurements of seeded implants.

2.14. Cell preparation for SEM

Sample preparation for SEM imaging was described previously [36]. The cell-seeded specimens cultured for 7 days were fixed with 2.5 % glutaraldehyde in 0.1 M sodium cacodylate buffer for at least 24 h at 4 $^{\circ}$ C to preserve the structure of cells. Subsequently, the samples were immersed in 1 % osmium tetroxide solution in 0.1 M sodium cacodylate buffer for 1 h, followed by immersion in 1 % tannic acid solution in the same buffer for another hour. These steps served to retain the lipid, protein, and carbohydrate structure of cells, and enhance the contrast and staining. Then, samples were dehydrated with a series of aqueous ethanol solutions (20 %, 30 %, 40 %, 50 %, 60 %, 70 %, 90 %, 96 % and 100 %). After dehydration, the samples were rinsed with hexamethyldisilazane (HMDS), a drying agent, and then left to air dry, allowing complete removal of any residual moisture. Prior to observation under SEM, the specimens were sputter-coated with gold nanoparticles.

2.15. Statistical analysis

For comparing the mechanical properties between different groups, statistical analysis was performed with one-way analysis of variance (ANOVA) with Tukey's post hoc multiple comparison tests. A p-value smaller than 0.05 was considered statistically significant.

3. Results

3.1. Rheological properties of inks

The rheological properties of the PCL/LP polymer nanocomposite inks are shown in Fig. 3. The shear viscosity curves were fitted to the Carreau model and the zero-shear viscosity η_0 and power index n are calculated and shown in Table 1. All inks show shear-thinning behaviour reflected by the viscosity decrease with increasing shear rate (Fig. 3 (A))

and a power index n smaller than 1 (Table 1). This behaviour is desirable for 3D printing as it facilitates extrusion. LP loading increases the zero-shear viscosity η_0 effectively (Fig. 3 (B)), and enhances the shear-thinning behavior, reflected by the decrease of the power index n. LP particle clustering at low shear rates can restrain the long-range motion of polymer chains, increasing the shear resistance [39]. Increasing the shear rate can result in the shape relaxation of LP particles (aligning with the flow), and the disentanglement of polymer chains of PCL, contributing to the decrease of viscosity and shear-thinning behaviour.

The storage modulus G' of PCL/LP inks was measured with frequency sweep tests (Fig. 3 (A)). The PCL/LP composite inks exhibit a plateau of storage modulus at low frequency, which is attributed to the percolation of the nanofillers and the formation of a robust interconnected nanofiller network of LP particles within the PCL matrix [40,41]. As the LP concentration increases, the plateau becomes more prominent, indicating a stronger interconnected nanofiller network. The storage modulus G' also increases throughout the frequency range as the LP concentration increases. This may also contribute to the increase in zero-shear viscosity as nanofiller loading concentration increases.

The relaxation time τ was estimated from the modulus crossover in frequency sweep tests (Table 1). With higher Laponite nanoclay concentrations, the relaxation time of the ink increases, indicating a longer time to release the stored stress and transition from a more elastic state into a more relaxed and viscous state. This is likely due to the combination of the restraint on the motion of the polymer chain and a more robust interconnected network, as mentioned above.

3.2. FTIR analysis

The FTIR spectra of the LP nanoclay filler, 3D-printed PCL, and PCL/30LP composites are shown in Fig. 4. In the PCL/30LP spectrum, the presence of Laponite is confirmed by the characteristic peak near 1000 cm⁻¹, corresponding to the Si–O stretching vibration of the tetrahedral sheet. A slight shift in the maximum of the C–O–C stretching band (approximately 1160 cm⁻¹) and carbonyl (C=O) stretching region (~1720 cm⁻¹) towards higher wavenumber is observed in PCL/30LP comparing to Pure PCL (Fig. 4). The peak of C–O–C stretching band in PCL/30LP is also sharper. These are associated with enhanced crystallinity and polymer chain ordering, as similar spectral changes have been linked to enhanced molecular ordering in semi-crystalline polymers [42]. No substantial shift towards the lower wavenumber was observed to support significant hydrogen bonding between PCL and Laponite.

3.3. Crystallinity assessment with DSC and XRD

The crystallinity of the 3D printed PCL/LP specimens with varying LP loading and printing orientation was assessed with both XRD and DSC. While XRD analyzes the intensity and distribution of diffracted Xrays by the crystalline regions, DSC quantifies the melting enthalpy of the specimen. The XRD patterns of PCL, Laponite, and PCL/30LP are shown in Fig. 5A. Two distinctive diffraction peaks can be identified in pure PCL at $2\theta = 21.3^{\circ}$ and 23.7° , which correspond to the orthorhombic planes (110) and (200), while the shoulder at $2\theta=22^{\circ}$ corresponds to the orthorhombic plane (111). In the range of 15°-30°, LP shows one visible peak at $2\theta = 20^{\circ}$ reflecting the plane (100). The peaks were deconvoluted to calculate the crystallinity of the 3D printed pure PCL specimens (Fig. 5 (B)) and PCL/LP polymer nanocomposite (Fig. 5 (C)), as shown in Fig. 5 (E). Examples of DSC thermograms of the specimens are shown in Fig. 5 (D), which was also used to calculate the crystallinity of 3D printed PCL/LP specimens as shown in Fig. 5 (F). Both DSC and XRD show the trend that the addition of LP nanoparticles increases crystallinity significantly when the loading density exceeds 10 %. LP particles acted as potential nucleation sites, enhancing the heterogeneous nucleation of crystalline regions in PCL [43]. This is also consistent with the FTIR results (Fig. 4). In addition, PCL/30LP specimens printed with 90° orientation have significantly higher crystallinity than

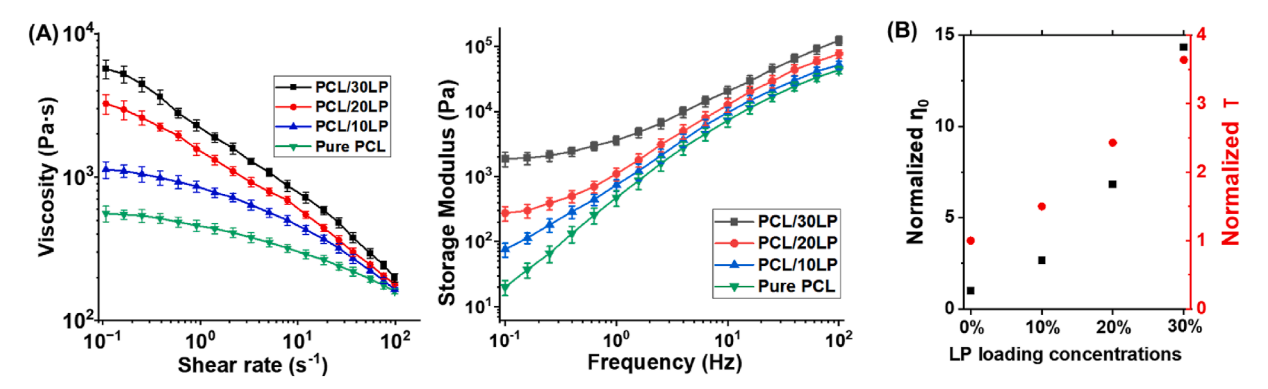


Fig. 3. Rheological properties of PCL/LP polymer composite inks. (A): Shear viscosity profile from flow sweep tests and storage modulus of PCL/LP inks with increasing LP density. (B) Effect of LP loading concentrations on the normalized zero-shear viscosity $η_0$ and normalized relaxation time τ compared to their values of pure PCL ink.

Table 1
Summary of rheological properties of PCL/LP inks comparing different LP loading concentrations.

Inks	Zero-shear viscosity η_0 (Pa·s)	Power index n	Relaxation time τ (ms)
Pure PCL	600	0.72	14
PCL/ 10LP	1600	0.59	21
PCL/ 20LP	4100	0.48	34
PCL/ 30LP	8600	0.36	51

those with 0° orientation, as discovered with DSC measurements. The lower exposure area of deposited filaments at 90° results in slower solidification and more time for the polymeric chains to develop into the crystal structure, which has been shown to increase crystallinity [44]. Between the two techniques of DSC and XRD, there is a slight difference

in the crystallinity measured due to their different principle (Fig. 5 (E) (F)). The crystallinity measured by DSC is slightly higher than that measured by XRD, which agrees with other studies [45,46].

3.4. Structural characterization

The structural characterization of the 3D printed specimens with different LP loading concentrations and printing orientations was conducted with SEM, micro-CT and AFM. The surface morphology of the gauge section of 3D printed dumbbell-shaped tensile specimens was characterized with SEM and micro-CT (Fig. 6AB). Between the two orientations, pure PCL, PCL/10LP and PCL/20LP specimens printed with 90° orientation show no visible interfaces between the filaments, indicating a good interfacial bonding. When printed with a 0° orientation, the filament interfaces are more recognizable through a distinct surface pattern aligned at 0°. As the LP loading concentration increases, the 0° surface pattern and interfaces between layers become more prominent. While shallow interfaces are seen on pure PCL specimens, all

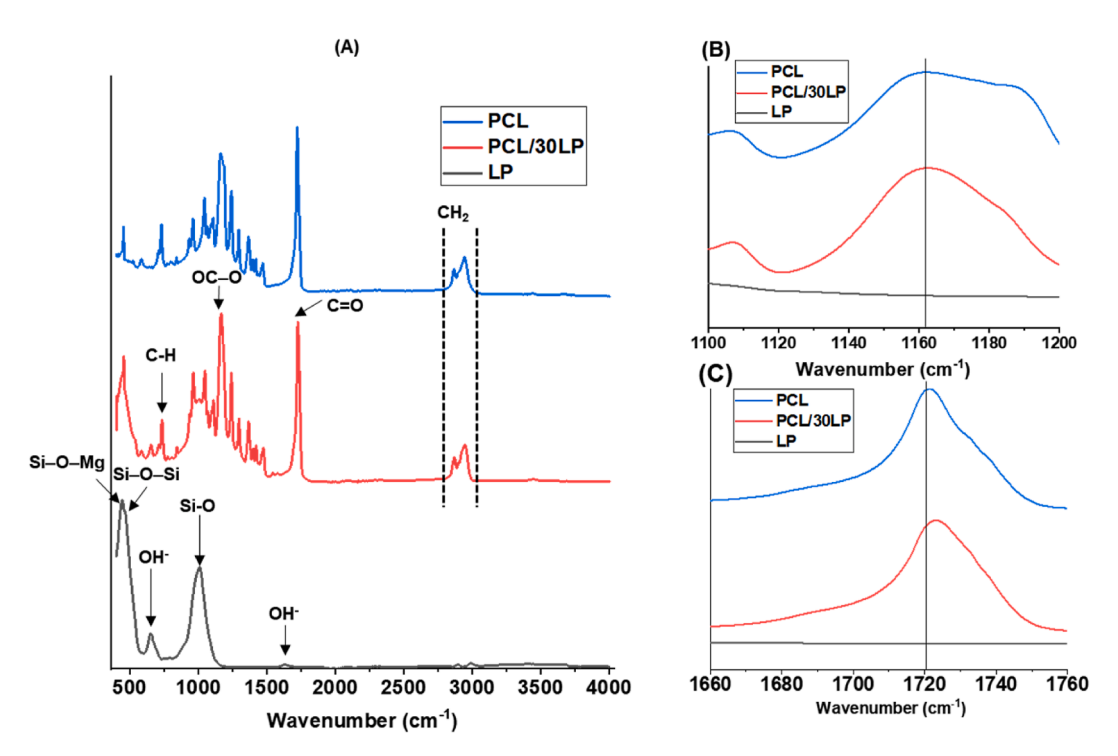


Fig. 4. FTIR spectra of LP nanoclay filler, 3D printed PCL, and PCL/30LP specimens across the wavenumber range of 500–4000 cm⁻¹ (A), 1660-1760 cm⁻¹ (B), and 1100–1200 cm⁻¹ (C). Key functional groups are labelled in (A), while slight shifts near 1160 (B) and 1720 cm⁻¹ (C) observed in the PCL/30LP composite are highlighted.

H. Chen et al. Biomedical Technology 11 (2025) 100101

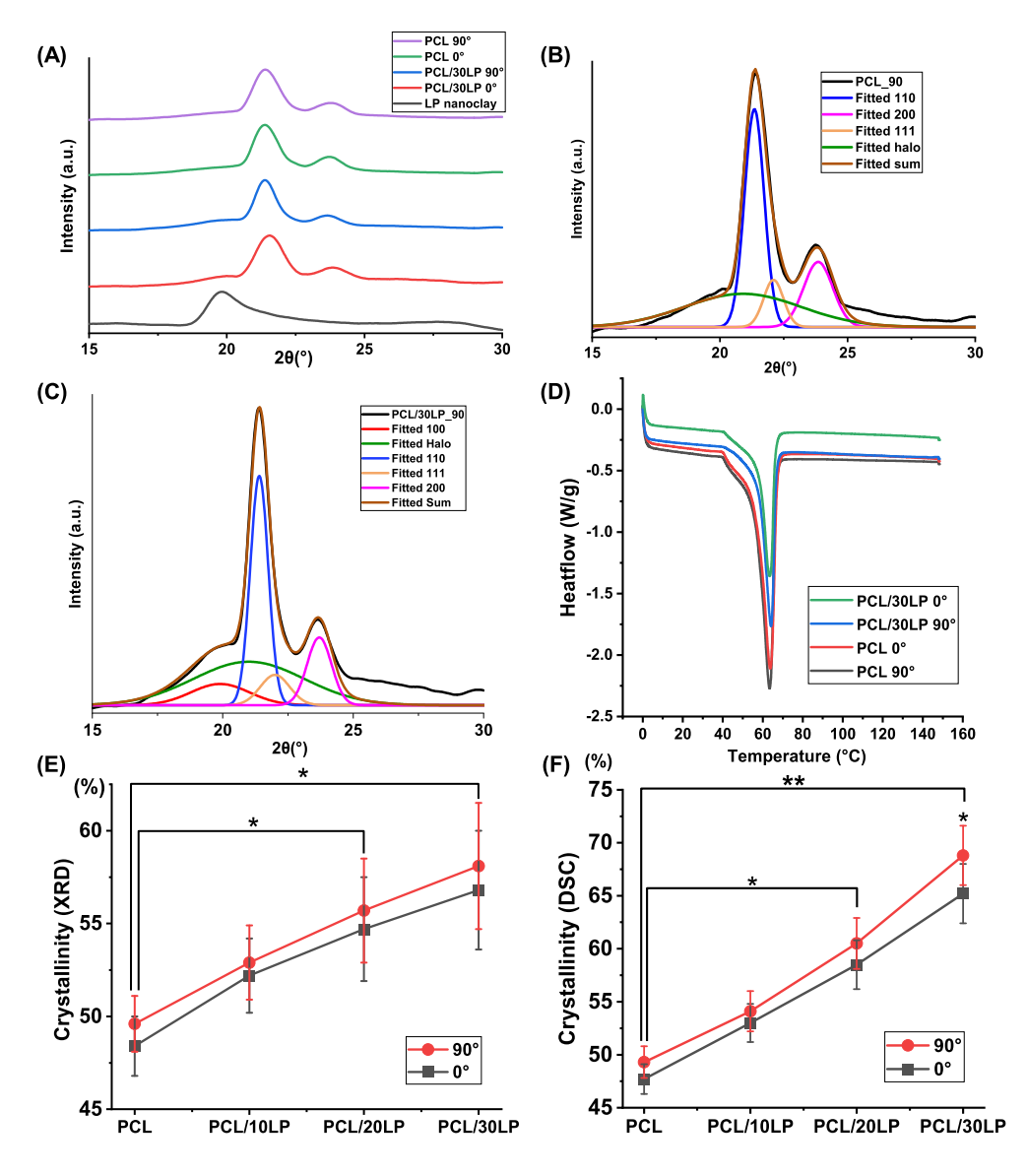


Fig. 5. XRD and DSC results of 3D printed PCL/LP specimens with two orientations (0° and 90°) for calculating crystallinity. (A) XRD peaks of PCL and PCL/30LP specimens with two orientations, (B) and (C): Deconvolution results of XRD peaks of PCL/30LP specimen with 90° orientation. The crystalline and amorphous phases of PCL were used for calculating its crystallinity (D) DSC curves of PCL and PCL/30LP specimens with two orientations (0° and 90°). Crystallinity of the specimens was calculated with both XRD (E) and DSC (F) measurements. The crystallinity of PCL/LP calculated from XRD peaks may be affected by the overlapping peaks of PCL and LP. Statistically significant differences were determined using an independent *t*-test as: *p < 0.05, and **p < 0.01.

4 layers are visible on PCL/30LP specimens with both orientations. Besides surface morphology, the 3D shape of the structure was also shown by micro-CT. PCL/30LP specimens have more prominent interfaces between layers than pure PCL specimens. In addition, PCL/30LP specimens maintain a more cuboid-like structure, while Pure PCL specimens have a more curved upper surface due to higher post-printing deformation.

Filament orientation impacts interfacial bonding due to differing nozzle travel times, which influences solvent evaporation and thus filament solidification. With 0° orientation, the increased nozzle traveling time between longer filaments extends the exposure area and time for deposited filaments before contacting adjacent ones. This results in enhanced solvent evaporation and solidification of deposited filaments. It reduces the post-printing deformation that flattens and merges filaments from gravity and capillary forces and thus preserves their cylindrical shape. Additionally, it reduces the interfacial bonding strength between filaments as they solidify before adjoining. In contrast, specimens printed with 90° exhibit better bonding between filaments due to shorter nozzle traveling distance between filaments. Such interfaces between filaments and layers within the structure can form air gaps [47]. They can be visualized from cross-sectional views of the micro-CT

scans as shown in Figure S3, and the porosity of the specimens (0.3 %–6.8 %) is shown in Figure S4B. Specimens printed at 0° show higher porosity than those at 90° , likely due to more pronounced filament interfaces that trap air. Within the same orientation, porosity also increases with higher nanofiller concentrations.

Increasing nanofiller (LP) concentration enhances the shape retention of filaments by improving the rheological properties of inks. Higher LP concentration boosts the inks' zero-shear viscosity η_0 , storage modulus G', and relaxation time τ , which collectively resist the aforementioned post-printing deformation prior to solidification (solvent evaporation). Additionally, higher LP concentration decreases solvent concentration, accelerating solvent evaporation and solidification, further decreasing the post-printing deformation. Due to their high surface energy, nanoparticles tend to agglomerate [48]. The size distribution of the LP clusters (>20 μ m) in 3D printed specimens assessed with micro-CT (Figure S4) shows that increasing LP concentration leads to fewer small clusters (<35 μ m) and more large clusters (>40 μ m). The median cluster size increases from 21 μ m to 26 μ m, likely due to more frequent particle collisions and interactions.

The surface roughness of the printed specimens was evaluated at both the nanoscale (via AFM) and microscale (via 3D microscopy), as

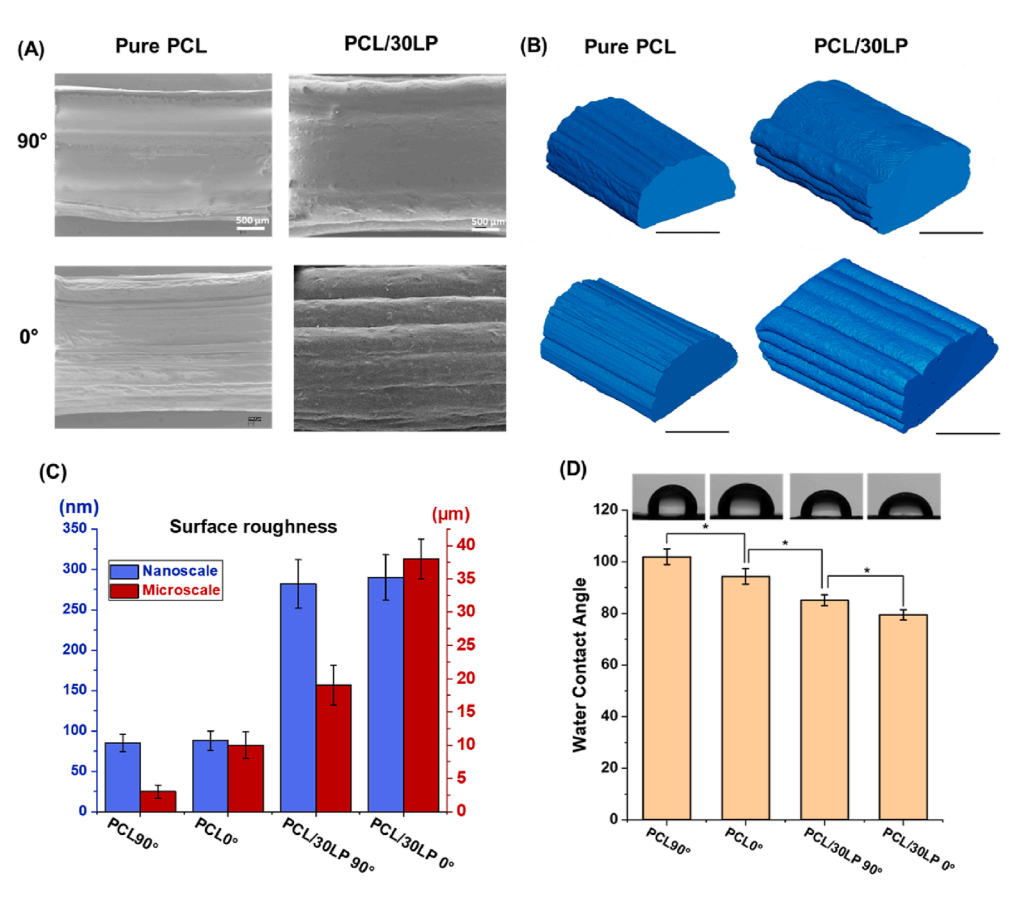


Fig. 6. Structural characterization of the reduced section of the specimens comparing the two orientations and nanofiller loading concentrations, and their wettability. (A) SEM images of the top view (scale bar 500 μ m) (B) 3D visualization from micro-CT results (scale bar: 2 mm). As nanofiller loading concentration increases, the filaments and layers become more visible, and the surface patterns become more prominent. (C) Nanoscale and microscale surface roughness (root mean square) of the specimens (D). Water contact angle measurements of the specimens.

shown in Fig. 6C. Neat PCL samples exhibited low roughness values, with PCL 90° measuring 85 nm/3 μm and PCL 0° at 88 nm/10 μm . In contrast, PCL/30LP samples showed a substantial increase in roughness, reaching 282 nm/19 μm (90°) and 290 nm/38 μm (0°). This increase in roughness is attributed to the presence and partial surface exposure of Laponite nanodisks and clusters. While print orientation had little effect on nanoscale roughness, the 0° orientation significantly increased microscale roughness due to more defined filament patterning from filament interfaces, as described earlier.

Alongside increased surface roughness, changes in wettability were observed by water contact measurements (Fig. 6D). The neat PCL printed at 90° exhibited the highest contact angle of 101.9° , reflecting its hydrophobic surface. The neat PCL printed at 0° reduced the contact angle to 94.3° , suggesting that the microscale surface patterning from printing at 0° enhances its wettability. With the addition of Laponite, a further reduction in contact angle was observed, which is attributed to the exposure of hydrophilic hydroxyl groups on Laponite surfaces [49], and the increased surface roughness. The PCL/30LP sample printed at 90° showed a contact angle of 85.0° , while the PCL/30LP printed at 0° exhibited the lowest value at 79.4° , indicating a marked improvement in surface wettability.

3.5. Mechanical properties

The Young's modulus (E), ultimate tensile strength (UTS), and fracture strain (FS) of the specimens were determined from their stress-strain curves (Figure S6) and shown in Fig. 7. Specimens with 90° orientation exhibit higher E, UTS, and FS than 0° orientation specimens, except for pure PCL, where no significant difference is found between the E of the two orientations. Young's modulus (E) increased significantly (up to 110 %) with increasing LP loading concentration. This

indicates a strong polymer-nanoparticle connection within the composite for stress dissipation [50] The crystallinity of PCL increased with the addition of LP, which can also contribute to the higher *E*, as intermolecular bonding in the crystalline phase is stronger [51,52]. The interconnected nanofiller network of LP within the PCL matrix can also have a reinforcement effect [53]. UTS and FS reduce significantly as LP loading concentration increases. The decrease in FS can be partly due to the reduced mobility of PCL polymer chains during the necking process, resulting from both higher crystallinity and higher LP nanoparticle loading concentrations [54].

The fracture morphology of the specimens with different printing orientations and nanofiller loading concentrations after tensile testing was characterized with micro-CT to further reveal their effect on mechanical properties (Fig. 8). As the nanofiller loading concentration increases, the fracture section is bigger due to reduced necking process and FS, which can be attributed to the structural characteristics. The nanofiller loading enhances the higher shape retention of deposited filaments and thus the interface between them, as seen in Fig. 6. These interfaces can affect stress distribution, leading to early breakages on PCL/30LP specimens (Fig. 8A). In addition, printing with 0° orientation and increasing nanofiller concentration has shown to increase the porosity of the structure, which can also contribute to such early breakages.

The increased rate and size of agglomerates with higher nanofiller concentration could affect the stress dissipation between the polymer matrix and concentrate stress [34,55]. Higher LP loading also raises the ink's zero-shear viscosity, strengthening the nanofiller network and reducing cluster mobility and fragmentation. Such agglomerations can debond from the matrix under high tensile load, inducing void formation as shown in Fig. 8B. LP agglomerations are found inside voids on the surface in SEM images. Micro-CT results revealed that a number of LP clusters are also exposed at the fracture site, indicating debonding. In

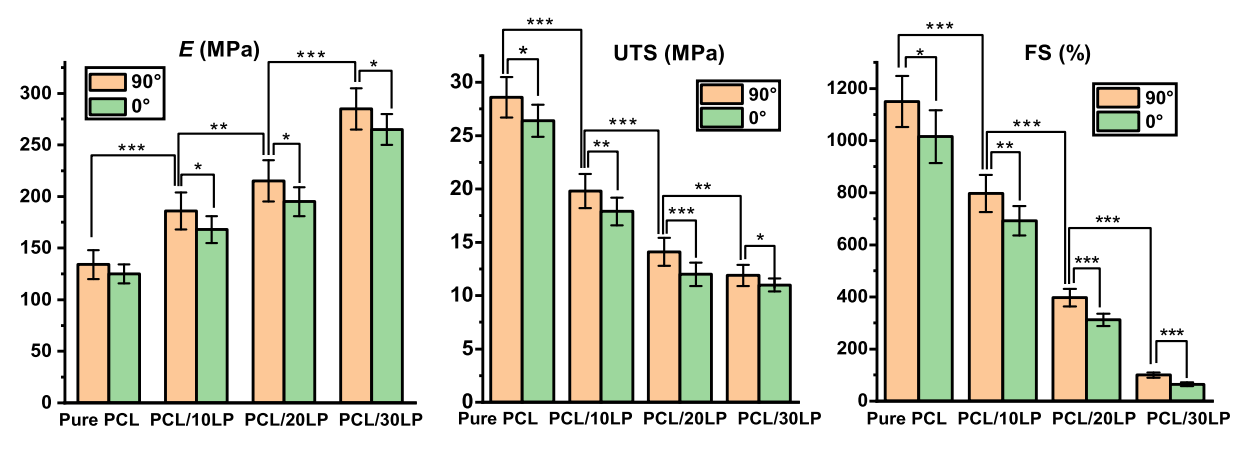


Fig. 7. Tensile properties including Young's modulus (E), ultimate tensile strength (UTS), and fracture strain (FS) of 3D printed specimens comparing 2 filament orientations (90° and 0° orientation) and different LP nanofiller loading concentration (0 %, 10 %, 20 %, 30 %). Statistically significant differences were determined using an independent t-test as: *p < 0.05, **p < 0.01, and ***p < 0.001.

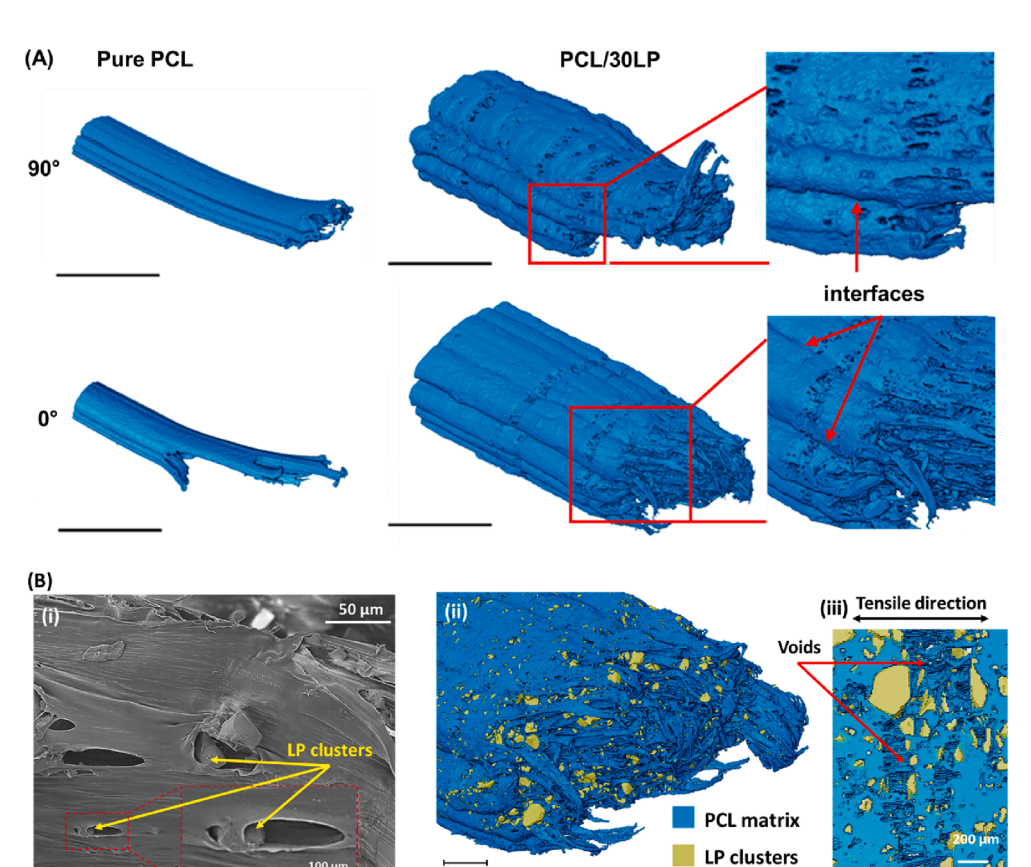


Fig. 8. Structural evaluation of the fracture morphology of the gauge section of 3D printed dumbbell-shaped tensile specimens after tensile testing comparing the two orientations and two inks. (A) 3D visualization of from micro-CT results (scale bar: 2 mm). The interfaces between layers and filaments on PCL/30LP specimens were highlighted in the separate zoomed-in images. (B) Evaluation of voids and LP clusters at the fracture sites. (i) SEM image of voids near a fracture site of the PCL/20LP specimen. 3D visualization (ii) from micro-CT results of PCL/ 30LP shows the PCL matrix in blue and exposed LP clusters in yellow, and crosssectional view (iii) of a fracture site.

addition, the cross-sectional view has shown LP clusters on both sides of some voids in the tensile direction, indicating possible breakage of clusters under tensile force.

3.6. In vitro assessment

In vitro assessment with HOB cells was conducted on the pure PCL and PCL/30LP specimens with 90° and 0° orientations. HOB cells were seeded on the 3D printed pure PCL and PCL/30LP structures with two orientations for 7 days, and their viability and deposition were assessed with live/dead assay and SEM (Fig. 9). HOB cells have shown high

viability (>97 %) on all specimens, proving their biocompatibility (Fig. 9 (A)). Cells were observed to attach in alignment with the filaments and tended to avoid the interfaces between filaments. For 0° orientation, the alignment of cell attachment followed the direction of printing (marked in yellow line in Fig. 9 (B), indicating that the 0° surface pattern acted as a directional cue to guide the growth of HOB cells. The orientation of cells tends to also align with the printing orientation. For the structures printed with 90° orientation, there was no visible cell alignment, as no obvious surface patterns were present.

LP nanoparticles tend to form agglomerates due to interactions between opposite charges on the faces (negative charge) and the edges (positive charge) of their disk shape [56]. The cell interaction with LP agglomerates has also been assessed using SEM, as shown in Fig. 9C. Cells surround a cluster of LP particles and have formed numerous filopodia on the LP cluster. This indicates that LP clusters have potentially attracted HOB cells and enhanced cell attachment, which in turn could boost overall bioactivity. PCL/30LP specimens have also significantly higher swelling ratio (Figure S7), surface roughness and wettability than pure PCL specimens, which can contribute to a more favorable environment for cell attachment and growth. This finding encourages further investigation into osteogenesis and other bioactivity metrics. This is also consistent with other studies [57–59], showing that the addition of LP in polymer matrices enhances cell proliferation and osteogenesis.

The proliferation results from the alamarBlueTM test show that cell proliferation increased across all groups until day 4, after which it plateaued (Fig. 10). PCL/30LP specimens exhibited significantly higher metabolic activity compared to pure PCL specimens beyond day 4. This is consistent with the findings in Fig. 9C. Specimens printed with a 0° orientation exhibited greater proliferation than those with a 90° orientation, likely due to the surface patterns guiding cell attachment and the increase in surface roughness and wettability. These findings

suggest that both Laponite incorporation and 0° printing orientation synergistically enhance implant bioactivity and proliferation potential.

Mineralization was evaluated using the Alizarin Red S assay, as illustrated in Fig. 11. Qualitative analysis revealed increased red staining on structures cultured with HOB cells for 17 days compared to the blank control, with further intensification observed at 26 days. This indicates progressive deposition of a mineralized matrix by HOB cells over time. For quantitative assessment, calcium deposition measurements from unseeded (blank control) specimens were subtracted from those of seeded samples at days 17 and 26. The absorbance reading of implants was compared to the standard curve (Figure S8) to measure the Alizarin red S concentration and then calculate the calcium deposition. All samples showed increased calcium deposition at day 26 compared to day 17. PCL/30LP exhibited significantly higher calcium deposition than pure PCL. The enhanced bioactivity with Laponite incorporation is likely due to the sustained release of bioactive ions (Si⁴⁺ and Mg²⁺) [57, 64], exposure of hydrophilic -OH groups that promote protein adsorption and cell adhesion [65,66], and increased micro- and nanoscale surface roughness of the implants. This combination improves surface wettability, which is closely linked to better cell attachment, spreading, and osteogenic activity. Additionally, specimens printed at a

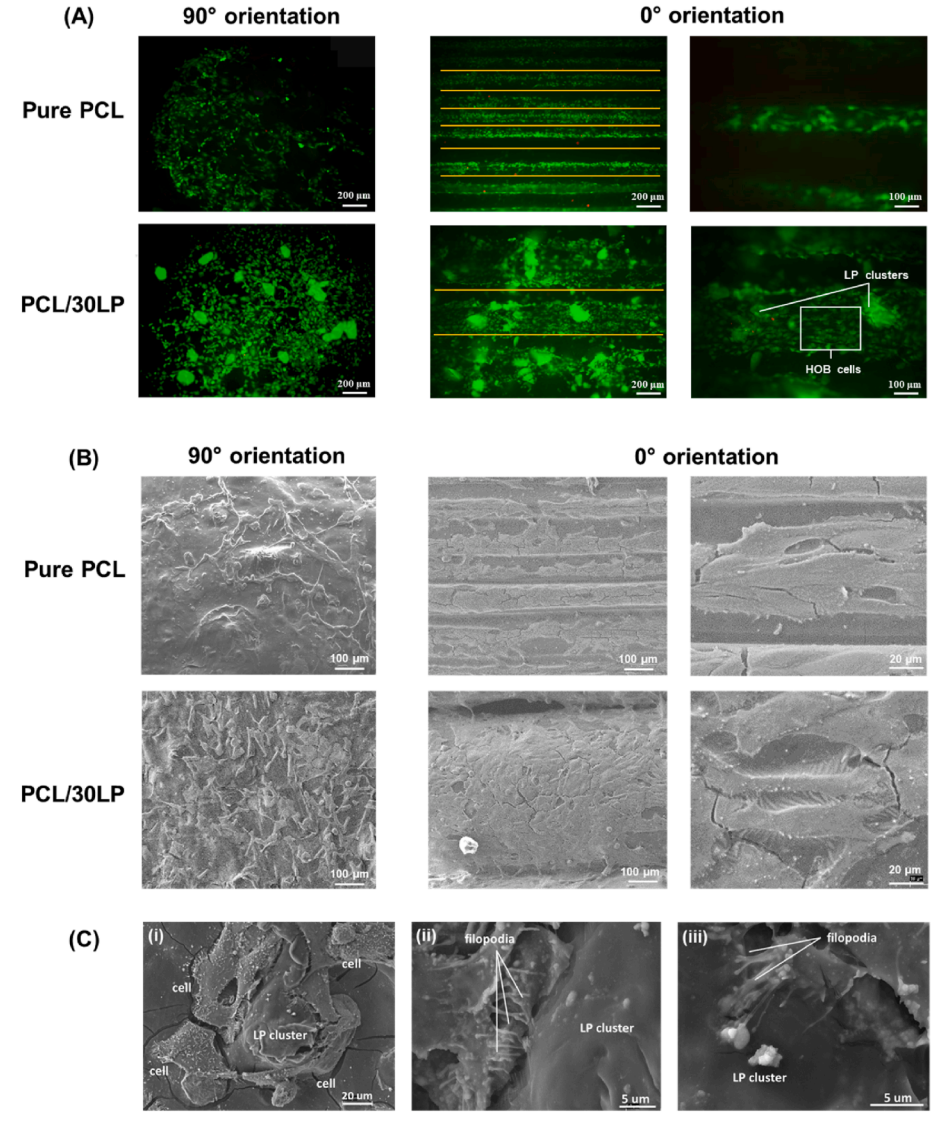


Fig. 9. Fluorescent and SEM images HOB cells cultured for 7 days on 3D printed pure PCL and PCL/ 30LP specimens with 90° and 0° orientations. (A) Fluorescent images of Live/Dead assay of 3D printed specimens. Live cells are shown in green while dead cells are shown in red. Yellow lines are the locations of the filament interfaces, which are in alignment with cell attachment. Contact guidance on cells was exhibited on specimens with 0° orientations while there is no obvious guidance on cell attachment on specimens with 90° orientation. (B) SEM images of HOB cells seeded on the specimens after 7 days. For 90° orientation, cells have attached to the filaments and avoided the interfaces and followed the pattern of 0° orientation. (C) SEM images showing the interaction between HOB cells and an LP cluster in a PCL/30LP specimen. (i): HOB cells have aggregated around and attached to an LP cluster. (ii) and (iii): The HOB cells have formed numerous filopodia around the LP cluster/.

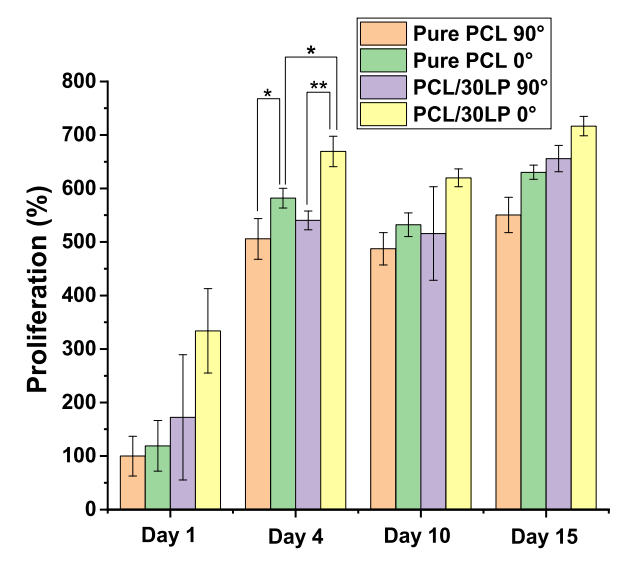


Fig. 10. Proliferation of HOB cells seeded on 3D printed pure PCL and PCL/30LP specimens with 90° and 0° orientations up to 15 days by alamarBlueTM assay. The results are normalized to Pure PCL 90° at day 1. Statistically significant differences are shown as $^*p < 0.05$, $^{**}p < 0.01$.

 0° orientation demonstrated greater calcium deposition compared to those printed at a 90° orientation using the same material. These results align with the observed proliferation trends, suggesting that incorporating LP and employing a 0° printing orientation significantly enhance both cell proliferation and mineralized matrix deposition.

4. Discussions

Shape fidelity of DIW 3D printing is often assessed in a 2D manner with microscopy, focusing on lattice structures predominantly. This study adopted a comprehensive 3D assessment using micro-CT on the shape retention and bonding of filaments, the particle cluster distribution and the air gaps within the printed implants. This approach revealed the relations between these variables and their collective impact on the mechanical properties and cell response of the printed structures.

Dumbbell-shaped specimens with a 90° orientation showed higher values of tensile properties compared to those printed at 0° . This is in contrast to FDM printing, where 0° orientation has shown enhanced mechanical properties [24–27]. Under tensile force, FDM-printed specimens with 90° orientation experienced delamination between filaments due to the perpendicular filament arrangement, which adversely affected their mechanical performance. Filaments with 0° orientation

were aligned towards the tensile loading direction resulting in higher tensile strength. These contrasting findings are likely due to the different speeds and nature of solidification between the two printing methods. FDM-printed filaments solidify quickly through cooling, leading to less post-printing deformation and more prominent interfaces, even at 90° orientation which are prone to delamination. In DIW printing, filaments solidify more gradually through solvent evaporation, resulting in stronger inter-filament bonding at 90° orientation with minimal visible interfaces. The shorter nozzle travel distance and reduced time between adjacent filaments in 90° orientation further enhance filament fusion and mechanical strength. In contrast, the greater spacing between filaments in 0° orientation leads to more distinct filament interfaces, which diminishes the expected mechanical advantage of filament alignment in the tensile loading direction.

As nanofiller loading concentration increases, Young's modulus E of the printed specimens increases significantly (up to 110 %) due to a robust polymer-nanoparticle connection and increased crystallinity, but FS and UTS decrease significantly. While the negative correlation between particle loading and tensile strength of the bulk material has also been observed in previous studies, such as by Bruyas et al. [60], the 3D assessment in the present study has elucidated this relationship. Higher concentrations of nanofillers enhance the shape retention of deposited filaments, which in turn affects both the interfaces and porosity. Additionally, it leads to an increase in the number and size of particle clusters, which also affects the dissipation of stress within the structure.

Compared to recent high-stiffness PCL composites, our DIWfabricated PCL/30LP implants (E \approx 285 MPa, UTS \approx 12 MPa, fracture strain ≈100 %) achieve a balanced mechanical profile combining moderate strength with high extensibility. Although Hashim et al. [61] reported grafted nanocellulose-reinforced PCL with higher stiffness (E = 661 MPa) and strength (UTS = 57 MPa), but the ductility (strain = 11 %) is low. Similarly, while Yan et al. [62] attained higher performance (E pprox530 MPa, UTS \approx 80 MPa) using continuous PA6 fibers in FDM-printed PCL, fracture strain is lower (~8.4 %) and fabrication was more complex. While DIW-printed neat PCL by Popescu et al. [63] showed high E (around 746 MPa) and UTS (around 17 MPa), but minimal elongation (<4 %). In comparison, the mechanical profile of our DIW-fabricated PCL/LP implants suggests improved energy absorption capacity while maintaining structural stability. The ~12 MPa tensile strength paired with ~100 % strain in this study indicates a high toughness, which may be advantageous in bone regeneration applications that benefit from mechanical compatibility with host tissue.

While post-printing deformation is traditionally deemed undesirable in 3D printing as it affects shape retention [15], the present work offers a new perspective by revealing its unexpected contributions to enhancing interfacial bonding and mechanical properties. It has shown to diminish the interface between the cylindrical filaments and improve filament bonding, and thus mechanical properties. This insight into the trade-off

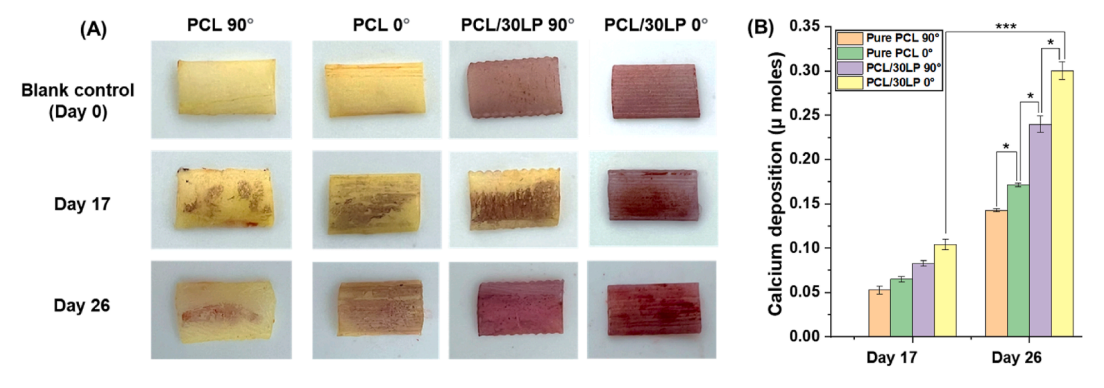


Fig. 11. Mineralization assessment of HOB cells seeded on 3D printed pure PCL and PCL/30LP specimens with 90° and 0° orientations for up to day 26 using Alizarin red S assay. (A) Qualitative assessment was shown with top-view images of the specimens post-staining. (B) Quantitative results are reported as u moles per well/specimen.

advocates a rethinking of shape retention and mechanical properties, and their integrated assessment for 3D printing tissue implants.

This study highlights the importance of cellular interactions in implant design, extending beyond structural and mechanical performance to address biological functionality relevant for clinical applications. Although the 0° orientation compromises mechanical properties due to prominent filament interfaces, it enhances surface wettability, and its surface patterning effect provides topographical cues that guide human osteoblast (HOB) alignment, mimicking native tissue architecture. Similarly, higher Laponite content, while reducing flexural strength and ultimate tensile strength, improves bioactivity by increasing nanofiller exposure, which attracts cells and promotes bonding. These trade-offs are reflected in the biological outcomes: PCL/ 30LP and 0° implants showed significantly higher metabolic activity and calcium deposition, suggesting a more osteoconductive environment.

This DIW-based strategy demonstrated effective control over both structural and biological performance, underscoring the critical interplay between ink composition, print design, and cellular response. Increasing Laponite content significantly enhanced ink viscosity, leading to improved shape retention and a 110 % increase in Young's modulus, indicating greater mechanical stability. Printing at 0° orientation produced filament-aligned surface features that guided osteoblast attachment and promoted directional cell growth. As a result, cell proliferation increased significantly after day 4, and calcium deposition was markedly higher by day 26 in PCL/30LP samples compared to neat PCL. These findings confirm that tuning ink formulation and printing orientation enables precise modulation of implant structure, mechanics, and bioactivity.

This technology shows promise for clinical use in applications requiring customized, surface-active implants. In craniomaxillofacial reconstruction, DIW-printed constructs can be tailored to patient-specific geometries while providing mechanical stability and surface features that promote osteoblast activity. Similarly, in alveolar ridge augmentation, these implants could serve as space-maintaining, bioactive barriers that support localized bone regeneration. The ability to tune structure, mechanics, and bioactivity highlights the potential for point-of-care or lab-side fabrication in non-load-bearing orthopaedic contexts.

Looking forward, this DIW platform could benefit from integration with other emerging technologies. Machine learning could accelerate ink formulation and print parameter optimization, while advanced biomaterials, such as responsive or degradable fillers, could enable dynamic implant behavior. Combining printed implants with embedded sensors or wearable devices could enable real-time monitoring and adaptive bone regeneration, advancing personalized and point-of-care treatment strategies.

5. Conclusions

This study presents a tunable design framework for engineering DIWprinted PCL/Laponite composites by systematically adjusting ink formulations and printing orientations to control shape fidelity, mechanical performance, and cellular response. In contrast to the FDM printing technique [24-27], DIW-printed dumbbell specimens with 90° orientation were found to exhibit significantly higher tensile properties than those with 0° orientation due to better interfacial bonding. Printing with a 0° orientation improves shape retention, generates surface patterns that guide cell attachment, and enhances cell proliferation and mineralization. Similarly, increasing Laponite concentration raises ink viscosity, further enhances shape retention, surface roughness, wettability, mechanical modulus, and cell proliferation and mineralization. It decreases tensile strength due to agglomeration effects and enhanced filament interfaces and porosity. This study reveals the complex interplay among material properties, printing orientation, structural integrity, mechanical attributes, and cellular interactions for 3D printing of tissue implants.

CRediT authorship contribution statement

Hongyi Chen: Writing - review & editing, Writing - original draft, Visualization, Validation, Software, Methodology, Investigation, Formal analysis, Data curation, Conceptualization. Rui Cheng: Writing - review & editing, Validation, Methodology, Investigation, Formal analysis. Se Hun Chung: Writing - review & editing, Validation, Methodology, Investigation, Formal analysis, Data curation, Conceptualization. Arsalan Marghoub: Writing – review & editing, Validation, Methodology, Investigation, Formal analysis. Hui Zhong: Formal analysis, Writing review & editing. Guohao Fang: Formal analysis, Writing - review & editing. Stavroula Balabani: Writing - review & editing, Validation, Methodology, Investigation, Formal analysis. Lucy Di-Silvio: Writing review & editing, Validation, Supervision, Project administration, Methodology, Investigation, Formal analysis, Data curation. Jie Huang: Writing – review & editing, Validation, Supervision, Resources, Project administration, Methodology, Investigation, Formal Conceptualization.

Ethical statement

This study does not involve human participants or animal experimentation. While we have used human osteoblast cells (PromoCell Catalogue No: C-12720), the cells are from a commercial source and were purchased. Therefore, ethical approval is not required. This study does not involve human participants.

Data availability

Data will be made available on request.

Declaration of competing interest

The authors declare that they have no known competing financial interests or personal relationships that could have appeared to influence the work reported in this paper.

Acknowledgement

Support from the Engineering and Physical Sciences Research Council (EPSRC) Manufacturing the Future programme (no. EP/N024915/1) to SB for part of this work is gratefully acknowledged.

Appendix ASupplementary data

Supplementary data to this article can be found online at https://doi.org/10.1016/j.bmt.2025.100101.

References

- [1] Y.Y.C. Choong, H.W. Tan, D.C. Patel, et al., The global rise of 3D printing during the COVID-19 pandemic, Nat. Rev. Mater. 5 (9) (2020) 637–639, https://doi.org/ 10.1038/s41578-020-00234-3.
- [2] Z. Wang, X. Liu, T. Ye, et al., 3D-printed perfused models of the penis for the study of penile physiology and for restoring erectile function in rabbits and pigs, Nat. Biomed. Eng. (2025), https://doi.org/10.1038/s41551-025-01367-y.
- [3] J. Li, D. Liang, X. Chen, W. Sun, X. Shen, Applications of 3D printing in tumor treatment, Biomed. Technol. 5 (2024) 1–13, https://doi.org/10.1016/j. bmt.2023.03.002.
- [4] H. Chen, S. Bansal, D.M. Plasencia, et al., Omnidirectional and multi-material in situ 3D printing using acoustic levitation, Adv. Mater. Technol. 10 (9) (2025) 2401792, https://doi.org/10.1002/admt.202401792.
- [5] H. Chen, J. Hardwick, L. Gao, D.M. Plasencia, S. Subramanian, R. Hirayama, Acoustics in additive manufacturing: a path toward contactless, scalable, and highprecision manufacturing, Appl. Phys. Rev. 12 (3) (2025), https://doi.org/10.1063/ 5.0271688.
- [6] H. Chen, Y. Liu, S. Balabani, R. Hirayama, J. Huang, Machine learning in predicting printable biomaterial formulations for direct ink writing, Research 6 (2023) 197, https://doi.org/10.34133/research.0197.

- [7] M.A.S.R. Saadi, A. Maguire, N.T. Pottackal, et al., Direct ink writing: a 3D printing technology for diverse materials, Adv. Mater. 34 (28) (2022) 2108855, https://doi. org/10.1002/adma.202108855.
- [8] Z. Liu, J. Huang, D. Fang, et al., Material extrusion 3D-printing technology: a new strategy for constructing water-soluble, high-dose, sustained-release drug formulations, Mater. Today Bio 27 (2024) 101153, https://doi.org/10.1016/j. mtbio.2024.101153.
- [9] H. Chen, 3D Printing Hybrid Scaffold with Hydrogel and filler-loaded PCL for Osteochondral Tissue Engineering, UCL (University College London), 2023.
- [10] H. Chen, J. Khong, J. Huang, Direct ink writing of polycaprolactone/laponite composite for bone implants: 3D characterization using x-ray micro CT, Ortho. Proc. 103-B (SUPP 16) (2021) 74, 74.
- [11] A. Zimmerling, Z. Yazdanpanah, D.M.L. Cooper, J.D. Johnston, X. Chen, 3D printing PCL/nHA bone scaffolds: exploring the influence of material synthesis techniques, Biomater. Res. 25 (1) (2021) 3, https://doi.org/10.1186/s40824-021-00204-v.
- [12] C. Darroch, G.A. Asaro, C. Gréant, et al., Melt electrowriting of a biocompatible photo-crosslinkable poly(D,L-lactic acid)/poly(ε-caprolactone)-based material with tunable mechanical and functionalization properties, J. Biomed. Mater. Res. 111 (6) (2023) 851–862, https://doi.org/10.1002/jbm.a.37536.
- [13] H. Wang, X. Xu, Y. Qin, et al., Wet-electrospun porous freeform scaffold enhances colonisation of cells, Mater. Today Bio 33 (2025) 101997, https://doi.org/ 10.1016/j.mtbio.2025.101997.
- [14] A.K. Gaharwar, S.M. Mihaila, A. Swami, et al., Bioactive silicate nanoplatelets for osteogenic differentiation of human mesenchymal stem cells, Adv. Mater. 25 (24) (2013) 3329–3336, https://doi.org/10.1002/adma.201300584.
- [15] A. Schwab, R. Levato, M. D'Este, S. Piluso, D. Eglin, J. Malda, Printability and shape fidelity of bioinks in 3D bioprinting, Chem. Rev. 120 (19) (2020) 11028–11055, https://doi.org/10.1021/acs.chemrev.0c00084.
- [16] H. Chen, T. Stampoultzis, A. Papadopoulou, S. Balabani, J. Huang, Evaluation of rheological properties and shape fidelity of polycaprolactone/hydroxyapatite inks for 3D printing of osteochondral tissue scaffolds, Ortho. Proc. 103-B (SUPP_2) (2021) 96, 96.
- [17] H. Chen, B. Zhang, J. Huang, Recent advances and applications of artificial intelligence in 3D bioprinting, Biophy. Rev. 5 (3) (2024), https://doi.org/10.1063/ 5.0190208
- [18] M. Das, A. Jana, R. Mishra, et al., 3D printing of a biocompatible nanoink derived from waste animal bones, ACS Appl. Bio Mater. 6 (4) (2023) 1566–1576, https:// doi.org/10.1021/acsabm.2c01075.
- [19] M. Das, R. Mishra, P. Das, et al., Controlled directionality in 3D printing of graphite-reinforced polymer composite with enhanced mechanical properties, Compos. Sci. Technol. 235 (2023) 109955, https://doi.org/10.1016/j. compscitech.2023.109955.
- [20] D. Yang, L. Li, H. Chen, C. Wang, J. Huang, T. Zheng, A rapid and bidirectional humidity-responsive actuator via one-step self-assembly of a PVDF@F127-TiO₂ monolithic membrane for smart wearables, Chem. Eng. J. 519 (2025) 165568, https://doi.org/10.1016/j.cej.2025.165568.
- [21] L. Zhang, B. Song, S.-K. Choi, Y. Shi, A topology strategy to reduce stress shielding of additively manufactured porous metallic biomaterials, Int. J. Mech. Sci. 197 (2021) 106331, https://doi.org/10.1016/j.ijmecsci.2021.106331.
- [22] X. Zhang, C. Liu, S. Wang, et al., Assessment of the mechanical and functional properties of nitinol alloys fabricated by laser powder bed fusion: effect of strain rates, Mater. Sci. Eng. 916 (2024) 147358, https://doi.org/10.1016/j. msea.2024.147358.
- [23] D. Huang, Z. Li, G. Li, et al., Biomimetic structural design in 3D-printed scaffolds for bone tissue engineering, Mater. Today Bio 32 (2025) 101664, https://doi.org/ 10.1016/j.mtbio.2025.101664.
- [24] J. Kiendl, C. Gao, Controlling toughness and strength of FDM 3D-printed PLA components through the raster layup, Compos. B Eng. 180 (2020) 107562, https://doi.org/10.1016/j.compositesb.2019.107562.
- [25] B. Akhoundi, A.H. Behravesh, Effect of filling pattern on the tensile and flexural mechanical properties of FDM 3D printed products, Exp. Mech. 59 (6) (2019) 883–897, https://doi.org/10.1007/s11340-018-00467-y.
- [26] M. Somireddy, C.V. Singh, A. Czekanski, Analysis of the material behavior of 3D printed laminates via FFF, Exp. Mech. 59 (6) (2019) 871–881, https://doi.org/10.1007/s11340-019-00511-5.
- [27] S.R. Rajpurohit, H.K. Dave, Analysis of tensile strength of a fused filament fabricated PLA part using an open-source 3D printer, Int. J. Adv. Des. Manuf. Technol. 101 (5) (2019) 1525–1536, https://doi.org/10.1007/s00170-018-3047-x.
- [28] X. Zhang, T. Chang, H. Chen, et al., Optimizing laser parameters and exploring building direction dependence of corrosion behavior in NiTi alloys fabricated by laser powder bed fusion, J. Mater. Res. Technol. 33 (2024) 4023–4032, https://doi. org/10.1016/j.jmrt.2024.10.105.
- [29] S. Scholpp, L.A. Hoffmann, E. Schätzlein, T. Gries, C. Emonts, A. Blaeser, Interlacing biology and engineering: an introduction to textiles and their application in tissue engineering, Mater. Today Bio 31 (2025) 101617, https://doi. org/10.1016/j.mtbio.2025.101617.
- [30] L. Cassari, A. Zamuner, G.M.L. Messina, et al., Bioactive PEEK: surface enrichment of vitronectin-derived adhesive peptides, Biomolecules 13 (2) (2023) 246.
- [31] S. Li, Z. Man, K. Zuo, et al., Advancement in smart bone implants: the latest multifunctional strategies and synergistic mechanisms for tissue repair and regeneration, Bioact. Mater. 51 (2025) 333–382, https://doi.org/10.1016/j. bioactmat.2025.05.004.

- [32] A.B.G. de Carvalho, M. Rahimnejad, R.L.M.S. Oliveira, et al., Personalized bioceramic grafts for craniomaxillofacial bone regeneration, Int. J. Oral Sci. 16 (1) (2024) 62, https://doi.org/10.1038/s41368-024-00327-7.
- [33] I. Elgali, O. Omar, C. Dahlin, P. Thomsen, Guided bone regeneration: materials and biological mechanisms revisited, Eur. J. Oral Sci. 125 (5) (2017) 315–337, https://doi.org/10.1111/eos.12364.
- [34] M.A. Fanovich, J. Ivanovic, I. Zizovic, D. Misic, P. Jaeger, Functionalization of polycaprolactone/hydroxyapatite scaffolds with Usnea lethariiformis extract by using supercritical CO2, Mater. Sci. Eng. C 58 (2016) 204–212, https://doi.org/ 10.1016/i.msec.2015.08.024.
- [35] S. Nakagawa, K-i Kadena, T. Ishizone, et al., Crystallization behavior and crystal orientation of Poly(ε-caprolactone) homopolymers confined in nanocylinders: effects of nanocylinder dimension, Macromolecules 45 (4) (2012) 1892–1900, https://doi.org/10.1021/ma202566f.
- [36] H. Chen, G. Gonnella, J. Huang, L. Di-Silvio, Fabrication of 3D bioprinted Bi-Phasic scaffold for bone-cartilage interface regeneration, Biomimetics 8 (1) (2023) 87, https://doi.org/10.3390/biomimetics8010087.
- [37] D.J. Lee, H.C. Tseng, S.W. Wong, Z. Wang, M. Deng, C.-C. Ko, Dopaminergic effects on in vitro osteogenesis, Bone Res. 3 (1) (2015) 15020, https://doi.org/10.1038/ boneres 2015 20
- [38] R. Nørgaard, M. Kassem, S.I.S. Rattan, Heat shock-induced enhancement of osteoblastic differentiation of hTERT-Immortalized mesenchymal stem cells, Ann. N. Y. Acad. Sci. 1067 (1) (2006) 443–447, https://doi.org/10.1196/ appals 1354 063
- [39] A. Papadopoulou, J.J. Gillissen, H.J. Wilson, M.K. Tiwari, S. Balabani, On the shear thinning of Non-Brownian suspensions: friction or adhesion? J. Non-Newtonian Fluid Mech. 281 (2020) 104298 https://doi.org/10.1016/j.jnnfm.2020.104298.
- [40] K. Issaadi, A. Habi, Y. Grohens, I. Pillin, Effect of the montmorillonite intercalant and anhydride maleic grafting on polylactic acid structure and properties, Appl. Clay Sci. 107 (2015) 62–69, https://doi.org/10.1016/j.clay.2015.01.004.
- [41] M. El Achaby, F.Z. Arrakhiz, S. Vaudreuil, E.M. Essassi, A. Qaiss, M. Bousmina, Preparation and characterization of melt-blended graphene nanosheets-poly (vinylidene fluoride) nanocomposites with enhanced properties, J. Appl. Polym. Sci. 127 (6) (2013) 4697–4707, https://doi.org/10.1002/app.38081.
- [42] A. Hejna, M. Sulyman, M. Przybysz, M.R. Saeb, M. Klein, K. Formela, On the correlation of lignocellulosic filler composition with the performance properties of Poly(ε-Caprolactone) based biocomposites, Waste Biomass Valor. 11 (4) (2020) 1467–1479, https://doi.org/10.1007/s12649-018-0485-5.
- [43] Q. Lv, C. Xu, D. Wu, Z. Wang, R. Lan, L. Wu, The role of nanocrystalline cellulose during crystallization of poly(e-caprolactone) composites: nucleation agent or not? Compos. Appl. Sci. Manuf. 92 (2017) 17–26, https://doi.org/10.1016/j. compositesa.2016.10.035.
- [44] L. Pigliaru, M. Rinaldi, L. Ciccacci, et al., 3D printing of high performance polymer-bonded PEEK-NdFeB magnetic composite materials, Funct. Compos. Mater. 1 (1) (2020) 4, https://doi.org/10.1186/s42252-020-00006-w.
- [45] M. Doumeng, L. Makhlouf, F. Berthet, et al., A comparative study of the crystallinity of polyetheretherketone by using density, DSC, XRD, and raman spectroscopy techniques, Polym. Test. 93 (2021) 106878, https://doi.org/ 10.1016/j.polymertesting.2020.106878.
- [46] G. Konstantopoulos, P. Maroulas, D.A. Dragatogiannis, S. Koutsoumpis, A. Kyritsis, C.A. Charitidis, The effect of interfacial resistance and crystallinity on heat transfer mechanism in carbon nanotube reinforced polyethylene, Mater. Des. 199 (2021) 100420. https://doi.org/10.1016/j.matdes.2020.109420
- 109420, https://doi.org/10.1016/j.matdes.2020.109420.

 [47] Y. Lu, J. Song, X. Yao, M. An, Q. Shi, X. Huang, 3D printing polymer-based bolus used for radiotherapy, Int. J. Bioprint. 7 (4) (2021) 414, https://doi.org/10.18063/iib/v7i4/414
- [48] S. Shrestha, B. Wang, P. Dutta, Nanoparticle processing: understanding and controlling aggregation, Adv. Colloid Interface Sci. 279 (2020) 102162, https:// doi.org/10.1016/j.cis.2020.102162.
- [49] A. Selim, A.J. Toth, D. Fozer, K. Süvegh, P. Mizsey, Facile preparation of a Laponite/PVA mixed matrix membrane for efficient and sustainable pervaporative dehydration of C1–C3 alcohols, ACS Omega 5 (50) (2020) 32373–32385, https:// doi.org/10.1021/acsomega.0c04380.
- [50] G. Santagiuliana, O.T. Picot, M. Crespo, et al., Breaking the nanoparticle loading-dispersion dichotomy in polymer nanocomposites with the art of croissant-making, ACS Nano 12 (9) (2018) 9040–9050, https://doi.org/10.1021/ acspano.8b02877.
- [51] Q. Liu, S. Yuan, Y. Guo, et al., Modulating the crystallinity, mechanical properties, and degradability of poly(e-caprolactone) derived polyesters by statistical and alternating copolymerization, Polym. Chem. 10 (20) (2019) 2579–2588, https:// doi.org/10.1039/C9PY00274J, 10.1039/C9PY00274J.
- [52] T. Kida, T. Kimura, A. Eno, et al., Effect of ultra-high-molecular-weight molecular chains on the morphology, crystallization, and mechanical properties of polypropylene, Polymers 13 (23) (2021) 4222.
- [53] Y. Zare, K.Y. Rhee, Development of a model for modulus of polymer halloysite nanotube nanocomposites by the interphase zones around dispersed and networked nanotubes, Sci. Rep. 12 (1) (2022) 2443, https://doi.org/10.1038/ s41598-022-06465-4.
- [54] B. Tian, Z. Li, J. Li, et al., The effects of rubber nanoparticles with different polarities on thermal properties and foaming performance of polypropylene blends, RSC Adv. 10 (52) (2020) 31355–31362, https://doi.org/10.1039/ D0RA04486E, 10.1039/D0RA04486E.
- [55] M. Bhattacharya, Polymer nanocomposites—A comparison between carbon nanotubes, graphene, and clay as nanofillers, Materials 9 (4) (2016) 262.

- [56] A. Sheikhi, S. Afewerki, R. Oklu, A.K. Gaharwar, A. Khademhosseini, Effect of ionic strength on shear-thinning nanoclay-polymer composite hydrogels, Biomater. Sci. 6 (8) (2018) 2073–2083, https://doi.org/10.1039/c8bm00469b.
- [57] L. Yuan, J. Wei, S. Xiao, et al., Nano-laponite encapsulated coaxial fiber scaffold promotes endochondral osteogenesis, Regen. Biomater. 11 (2024) rbae080, https://doi.org/10.1093/rb/rbae080.
- [58] Z. Orafa, S. Irani, A. Zamanian, H. Bakhshi, H. Nikukar, B. Ghalandari, Coating of laponite on PLA nanofibrous for bone tissue engineering application, Macromol. Res. 29 (3) (2021) 191–198, https://doi.org/10.1007/s13233-021-9028-1.
- [59] Y. Zhang, W. Jiang, S. Yuan, Q. Zhao, Z. Liu, W. Yu, Impacts of a nano-laponite ceramic on surface performance, apatite mineralization, cell response, and osseointegration of a polyimide-based biocomposite, Int. J. Nanomed. 15 (null) (2020) 9389–9405, https://doi.org/10.2147/IJN.S273240.
- [60] A. Bruyas, F. Lou, A.M. Stahl, et al., Systematic characterization of 3D-printed PCL/ β-TCP scaffolds for biomedical devices and bone tissue engineering: influence of composition and porosity, J. Mater. Res. 33 (14) (2018) 1948–1959, https://doi. org/10.1557/imr.2018.112.
- [61] Hb Hashim, NAAb Emran, T. Isono, et al., Improving the mechanical properties of polycaprolactone using functionalized nanofibrillated bacterial cellulose with high

- dispersibility and long fiber length as a reinforcement material, Compos. Appl. Sci. Manuf. 158 (2022) 106978, https://doi.org/10.1016/j.compositesa.2022.106978.
- [62] Y. Yan, S. Sun, S. Pillay, H. Ning, Printability and mechanical behaviors of continuous polyamide fiber reinforced polycaprolactone composites, Polym. Compos. 46 (5) (2025) 4491–4505, https://doi.org/10.1002/pc.29254.
- [63] D. Popescu, C. Stochioiu, F. Baciu, M.C. Iacob, 3D-Printed polycaprolactone mechanical characterization and suitability assessment for producing wrist–hand orthoses, Polymers 15 (3) (2023) 576.
- [64] M. Ponjavic, M.S. Nikolic, J. Nikodinovic-Runic, S. Jeremic, S. Stevanovic, J. Djonlagic, Degradation behaviour of PCL/PEO/PCL and PCL/PEO block copolymers under controlled hydrolytic, enzymatic and composting conditions, Polym. Test. 57 (2017) 67–77, https://doi.org/10.1016/j. polymertesting.2016.11.018.
- [65] C. Gao, S. Peng, P. Feng, C. Shuai, Bone biomaterials and interactions with stem cells, Bone Res. 5 (1) (2017) 17059, https://doi.org/10.1038/boneres.2017.59.
- [66] A.K. Gaharwar, P.J. Schexnailder, B.P. Kline, G. Schmidt, Assessment of using laponite® cross-linked poly(ethylene oxide) for controlled cell adhesion and mineralization, Acta Biomater. 7 (2) (2011) 568–577, https://doi.org/10.1016/j. actbio.2010.09.015.